

Article

Alkali-Activated Materials as Catalysts for Water Purification

Anne Heponiemi , Janne Pesonen , Tao Hu  and Ulla Lassi 

Research Unit of Sustainable Chemistry, University of Oulu, P.O. Box 4300, FI-90014 Oulu, Finland; janne.pesonen@oulu.fi (J.P.); tao.hu@oulu.fi (T.H.); ulla.lassi@oulu.fi (U.L.)

* Correspondence: anne.heponiemi@oulu.fi

Abstract: In this study, novel and cost-effective alkali-activated materials (AAMs) for catalytic applications were developed by using an industrial side stream, i.e., blast furnace slag (BFS). AAMs can be prepared from aluminosilicate precursors under mild conditions (room temperature using non-hazardous chemicals). AAMs were synthesized by mixing BFS and a 50 wt % sodium hydroxide (NaOH) solution at different BFS/NaOH ratios. The pastes were poured into molds, followed by consolidation at 20 or 60 °C. As the active metal, Fe was impregnated into the prepared AAMs by ion exchange. The prepared materials were examined as catalysts for the catalytic wet peroxide oxidation (CWPO) of a bisphenol A (BPA) aqueous solution. As-prepared AAMs exhibited a moderate surface area and mesoporous structure, and they exhibited moderate activity for the CWPO of BPA, while the iron ion-exchanged, BFS-based catalyst (Fe/BFS30-60) exhibited the maximum removal of BPA (50%) during 3 h of oxidation at pH 3.5 at 70 °C. Therefore, these new, inexpensive, AAM-based catalysts could be interesting alternatives for catalytic wastewater treatment applications.

Keywords: alkali-activated material; geopolymer; blast furnace slag; catalytic wet peroxide oxidation; Fe-catalyst; bisphenol A



Citation: Heponiemi, A.; Pesonen, J.; Hu, T.; Lassi, U. Alkali-Activated Materials as Catalysts for Water Purification. *Catalysts* **2021**, *11*, 664. <https://doi.org/10.3390/catal11060664>

Academic Editor: Roberto Fiorenza

Received: 7 May 2021
Accepted: 22 May 2021
Published: 23 May 2021

Publisher's Note: MDPI stays neutral with regard to jurisdictional claims in published maps and institutional affiliations.



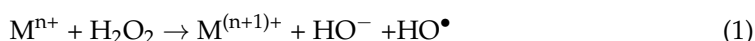
Copyright: © 2021 by the authors. Licensee MDPI, Basel, Switzerland. This article is an open access article distributed under the terms and conditions of the Creative Commons Attribution (CC BY) license (<https://creativecommons.org/licenses/by/4.0/>).

1. Introduction

Alkali-activated materials (AAMs) are inorganic, amorphous compounds that contain $[\text{SiO}_4]^{4-}$ and $[\text{AlO}_4]^{5-}$, which can be prepared by using aluminosilicates in addition to hydroxides, carbonates, or silicates of alkali and alkaline earth metals. The calcium content affects the AAM structure; therefore, materials with a low Ca content comprise a three-dimensional, highly interconnected aluminosilicate framework (also known as a geopolymer) [1], while those with a high Ca content comprise a cross-linked and non-cross linked structure that resembles that of tobermorite [2]. The use of AAMs, and especially geopolymers, has been investigated in the building industry as a more environment-friendly alternative to Portland cement, due to their chemical and physical stability [3–5], as well as in more advanced applications, such as adsorbents for the removal of impurities from wastewater [6–9] and composite materials [4]. Moreover, owing to the fact that the structure of AAMs is similar to that of zeolites, their use as catalytic materials can also be exploited. Compared with the synthesis of zeolites, that of AAMs can be performed at ambient pressure and room temperature, using cost-effective raw materials (kaolin clay or industrial waste, such as fly ash), making AAMs fascinating, environment-friendly alternatives to commercial zeolite. Only a few years ago, Sazama et al. reported the synthesis of AAM-based catalysts [10] by the modification of metakaolin geopolymers for the catalytic reduction of nitrogen oxides by ammonia, as well as the total oxidation of volatile hydrocarbons. Furthermore, metakaolin-based geopolymers and steel slag-containing AAMs also have been examined for photocatalytic applications [11,12] and biodiesel production [13]. Therefore, AAMs are interesting alternatives as catalysts, as well as for water-phase applications like catalytic wet peroxide oxidation (CWPO).

Bisphenol A (BPA) is an estrogenic compound commonly used in the production of polycarbonate plastic and epoxy resin, which are further utilized in several daily-use

plastic products, such as drinking bottles, containers, thermal paper, etc. [14]. BPA can be spread into water bodies during the manufacturing process, and also from daily-use plastic products. Due to its endocrine disrupting character for humans and environment [15], the removal of it from wastewaters is essential. Several techniques, such as activated sludge treatment [16], membrane bioreactors [17], and sorption [18,19] have been used for the removal of BPA from wastewaters. In addition of these, advanced oxidation processes (AOPs) have been effectively used for the oxidation of BPA in wastewaters [20]. Techniques like photolysis [21] and ozonation [22], as well as hybrid processes like UV/H₂O₂ [23], UV/O₃ [24], UV/TiO₂ [25], and O₂/H₂O₂ [26], have been successfully used for the oxidation of BPA. In this study, one of AOPs, CWPO, is studied for the removal of BPA from water. In CWPO, hydrogen peroxide is used as an oxidizing agent to decompose organic compounds from wastewater. Transition metals, typically Fe and Cu, are used as catalysts in the reaction to decompose hydrogen peroxide to active hydroxyl radicals (Equation (1)) [27].



The formed hydroxyl radicals can further oxidize organic compounds, according to Equation (2):



To obtain the reduced form of the active metals, they must be dispersed on suitable supports [28,29]. Various materials have been used as supports in CWPO. Carbon-based materials, such as activated carbon [30], graphite, carbon black [31], carbon nanotubes [32], and biomass-based carbons [33], have been successfully used for the degradation of organics with CWPO. Moreover, zeolites [34,35] and clay materials [36,37] also have been applied as supports for Fe and Cu; therefore, AAMs with a chemical composition similar to those of zeolites and clay minerals are interesting alternatives as carriers for use in CWPO.

However, for the use of industrial side streams as raw materials in a catalyst, the prepared material must exhibit stability, especially when the prepared material is used for water treatment applications. Typically, catalyst stability for photocatalytic experiments has been evaluated in consecutive tests [38] and by characterization of the used materials after experiments, e.g., by X-ray diffraction (XRD) and Fourier transform infrared spectroscopy (FTIR) [39,40].

In this study, the industrial side stream from the steel industry, i.e., blast furnace slag (BFS), was applied as a raw material to produce cost-effective catalytic materials for water purification. Catalysts were prepared by mixing different ratios of BFS and NaOH, followed by their consolidation at 20 °C and 60 °C. Moreover, iron was impregnated as the active metal in the AAMs via ion exchange. The as-prepared materials were characterized, e.g., by XRD, and their surface area and catalytic activity were examined for the CWPO of a bisphenol A (BPA) aqueous solution. Particular attention has been focused on the stability of materials; therefore, the possible leaching of the main elements (such as Ca, Si, Al, Mg, and Na) has been investigated before the CWPO of BPA under 2 MPa and 150 °C. Furthermore, the concentrations of the main elements of the as-prepared materials was analyzed after oxidation experiments from water samples, as well as those from the used catalysts.

2. Results and Discussion

In this section, the stability and characteristics, such as phase composition and specific surface area, of the prepared materials are discussed. In addition, the activity of AAMs for the CWPO of BPA is evaluated. The prepared materials were named according to their NaOH concentration and consolidation temperature (Section 3.1).

2.1. Stability of Alkali-Activated Materials

Table 1 lists the conductivity values of aqueous solutions after 4 h at 150 °C under an N₂ atmosphere of 2 MPa and an AAM concentration of 4 g/dm³.

Table 1. Conductivity of aqueous solutions after 4 h at 150 °C under an N₂ atmosphere of 2 MPa and AAM concentration of 4 g/dm³.

AAM	Conductivity [$\mu\text{S}/\text{cm}$]
BFS	533
BFS17.5-20	252
BFS17.5-60	332
BFS20-20	320
BFS20-60	288
BFS25-20	191
BFS25-60	166
BFS30-20	204
BFS30-60	195

The conductivity values of aqueous solutions after 4 h of experiments were 200–300 $\mu\text{S}/\text{cm}$; according to these values, the alkali activation of BFS stabilized the material. With the increase in the amount of NaOH in the sample, the conductivity of aqueous solutions decreased slightly. In addition, the curing temperature affected the conductivity, i.e., samples that were first cured at 60 °C for 24 h exhibited lower conductivity than those cured at room temperature.

Table 2 lists the concentrations of Ca, Si, and Al in aqueous solutions after 4 h at 150 °C, under an N₂ atmosphere of 2 MPa and an AAM concentration of 4 g/dm³.

Table 2. Ca, Si, and Al concentrations of aqueous solutions after 4 h at 150 °C, under an N₂ atmosphere of 2 MPa and an AAM concentration of 4 g/dm³.

AAM	Ca [mg/dm^3]	Si [mg/dm^3]	Al [mg/dm^3]
BFS17.5-20	29	16.0	2.6
BFS17.5-60	15	8.5	1.3
BFS20-20	20	9.6	1.8
BFS20-60	22	8.1	2.3
BFS25-20	34	7.7	3.5
BFS25-60	23	9.9	2.8
BFS30-20	27	12.0	4.9
BFS30-60	31	11.0	4.3

In addition to those of Ca, Si, and Al, Mg and Na concentrations also were analyzed from water samples by inductively coupled plasma–optical emission spectroscopy (ICP-OES). However, the magnesium concentration was less than the detection limit ($\leq 0.1 \text{ mg}/\text{dm}^3$), and the maximum sodium concentration was 1 mg/dm^3 after 4 h at 150 °C and an N₂ atmosphere of 2 MPa. All of the samples exhibited almost the same Ca and Si concentrations. However, with the increase in the amount of NaOH in the samples, the leaching of aluminum increased. Clearly, alkali activation immobilized Al in the inorganic matrix, but basicity enhanced its dissolution [41]. Furthermore, curing at room temperature led to the enhanced dissolution of Ca and Al from AAMs. A curing temperature of 60 °C has been found to be favorable for geopolymer preparation. Muñiz-Villarreal et al. [42] have reported that the optimum dissolution and formation of hydroxy species and oligomers, as well as further polymerization or condensation, occur at 60 °C. Therefore, with the increase in the curing temperature of the BFS-based AAMs, the leaching of Ca, Si, and Al decreased. Thus, based on these stability tests, AAMs that are first cured at 60 °C for 24 h are further characterized by XRD, diffuse-reflectance infrared Fourier transform spectroscopy (DRIFTS), field emission scanning electron microscope with energy-dispersive X-ray spectroscopy (FESEM-EDS), ICP-OES, and surface area techniques, as well as being examined for the CWPO of a BPA aqueous solution.

2.2. Characterization of AAMs

Table 3 lists the results of the Brunauer–Emmett–Teller (BET) surface areas of the prepared AAMs.

Table 3. BET-specific surface areas (SSA) and pore volumes (PV) of AAMs.

Sample	SSA [m ² /g]	PV [m ³ /g]
BFS	1.21	0.003
BFS17.5-20	19.5	0.081
BFS17.5-60	13.2	0.062
BFS20-20	14.6	0.077
BFS20-60	14.8	0.083
BFS25-20	11.0	0.047
BFS25-60	23.7	0.119
BFS30-20	26.5	0.112
BFS30-60	27.3	0.162
Fe/BFS17.5-60	38.0	0.120
Fe/BFS30-60	52.0	0.162

The specific surface area of BFS was negligible, while alkali activation led to the increased surface area of all samples (Table 3). Samples prepared by using the highest amount of NaOH exhibited the highest specific surface area, as well as the highest pore volume. Clearly, a low Si/Na ratio favored the formation of a porous structure in the samples. Sindhunata et al. [43] have reported the highest pore volume for fly-ash-based geopolymers at a SiO₂/Na₂O ratio < 1. Moreover, the samples cured at 60 °C for 24 h exhibited a slightly higher specific surface area, and hence a higher pore volume, than those prepared at room temperature. The higher curing temperature promoted the removal of excess water from the material structure, which in turn increased the porosity of samples further. Furthermore, higher curing temperatures (>50 °C) have been reported to particularly increase the amount of mesopores in the material [43].

As can be observed from the surface area results, no significant differences between the AAMs were observed. Therefore, to examine the effect of the Na concentration of samples on the catalytic behavior, samples with the lowest and highest Na concentration (BFS17.5-60 and BFS30-60) were selected as support materials for Fe catalysts. Surprisingly, the surface areas of the Fe catalysts were greater than those of the BFS17.5-60 and BFS30-60 pure supports (Table 3). This result was related to the calcination performed for Fe catalysts. During heat treatment, excess water and carbon dioxide of the support material, and well as traces of Fe salt, evaporated from the AAM structure, enabling the increase in the specific surface area [44]. In addition, the calcination of Fe catalysts led to the decomposition of hydrotalcite (Figure 1, XRD results), which also affected the surface area of materials [44]. Furthermore, as-prepared AAMs mainly exhibited a mesoporous structure (i.e., pore diameter between 2 and 50 nm), with ~10% of pores exhibiting a diameter of less than 2 nm. However, by the addition of Fe to BFS17.5-60 and BFS30-60 via ion exchange, the number of mesopores decreased to 80%, while micropores accounted for only a small percentage of the total pore volume. Moreover, macropores accounted for only ~15% of the total pore volume in Fe/BFS17.5-60 and Fe/BFS30-60, while before Fe ion exchange, pores greater than 50 nm were not detected (i.e., heat treatment enhanced the formation of large pores).

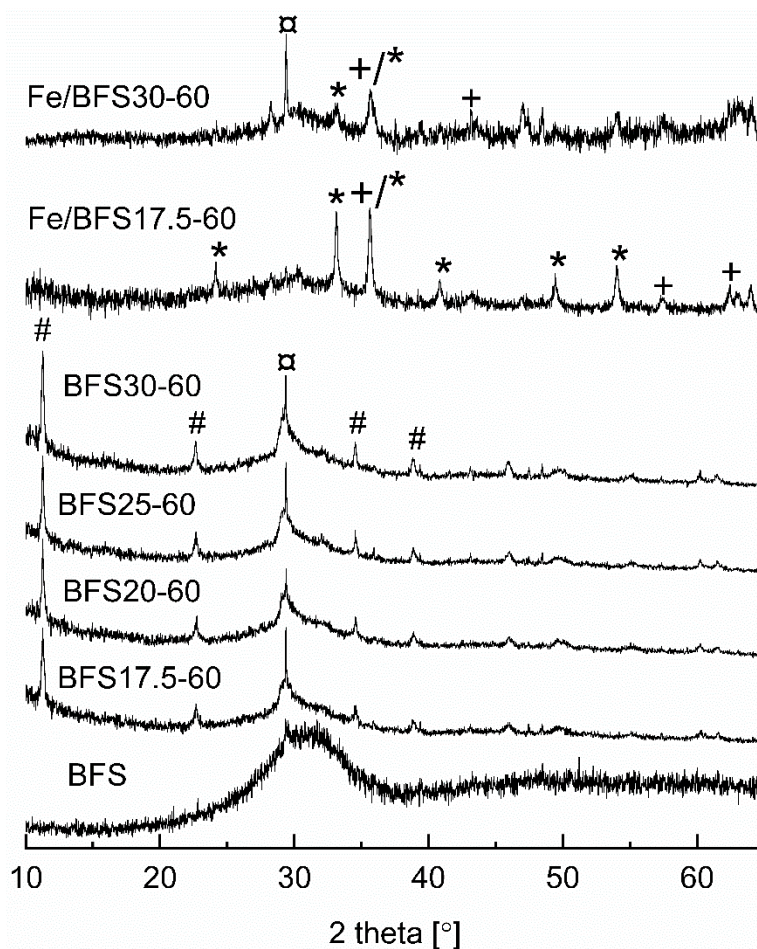


Figure 1. X-ray diffractograms of BFS raw material, supports, and Fe catalysts. (#) ICDD file 00-022-0700 ($\text{Mg}_6\text{Al}_2\text{CO}_3(\text{OH})_{16}\cdot 4\text{H}_2\text{O}$, hydrotalcite); (\square) ICDD file 01-083-4609 (CaCO_3); (*) ICDD file 04-015-7029 (Fe_2O_3); (+) ICDD file 04-008-8146 (Fe_3O_4).

Figure 1 shows the X-ray diffractograms of the BFS raw material; BFS17.5-60, BFS20-60, BFS25-60, and BFS30-60 supports; and Fe/BFS17.5-60 and Fe/BFS30-60 catalysts. In the X-ray diffractogram of BFS, crystal peaks were not observed, but only one wide halo at 2θ between 22° and 40° was observed, which is characteristic of an amorphous material. After the alkali activation of BFS with NaOH, peaks were observed at 2θ values of 11.3° , 22.8° , 34.5° , and 38.6° (denoted with #), corresponding to hydrotalcite ($\text{Mg}_6\text{Al}_2\text{CO}_3(\text{OH})_{16}\cdot 4\text{H}_2\text{O}$ (ICDD file 00-022-0700)), and the high-intensity peak at $\sim 29.4^\circ$ corresponded to CaCO_3 (ICDD file 01-083-4609). However, the broad “hump” observed at 2θ of $28\text{--}35^\circ$ was still present in the X-ray diffractograms of all supports, indicative of a partly amorphous structure. After the ion exchange of BFS17.5-60 and BFS30-60 with the Fe solution, the peaks observed at 2θ values of 24.1° , 33.2° , 35.6° , 40.9° , 49.5° , and 54.1° (denoted by *) and at 35.7° , 43.4° , 57.4° , and 63.0° (denoted by +) revealed the presence of Fe_2O_3 (ICDD file 04-015-7029) and Fe_3O_4 (ICDD file 04-008-8146) phases, respectively. Owing to the heat treatment of Fe catalysts, hydrotalcite was decomposed [44], and peaks corresponding to hydrotalcite were not observed in the X-ray diffractograms of Fe/BFS17.5-60 and Fe/BFS30-60.

Figure 2 shows the DRIFT spectra of BFS, BFS17.5-60, BFS30-60, Fe/BFS17.5-60, and Fe/BFS30-60. In the DRIFT spectrum of the BFS raw material, only a few peaks were observed. The band at $\sim 1420\text{ cm}^{-1}$ corresponded to Na_2CO_3 [45], and the strong peak at $\sim 1110\text{ cm}^{-1}$ corresponded to pure silica [46].

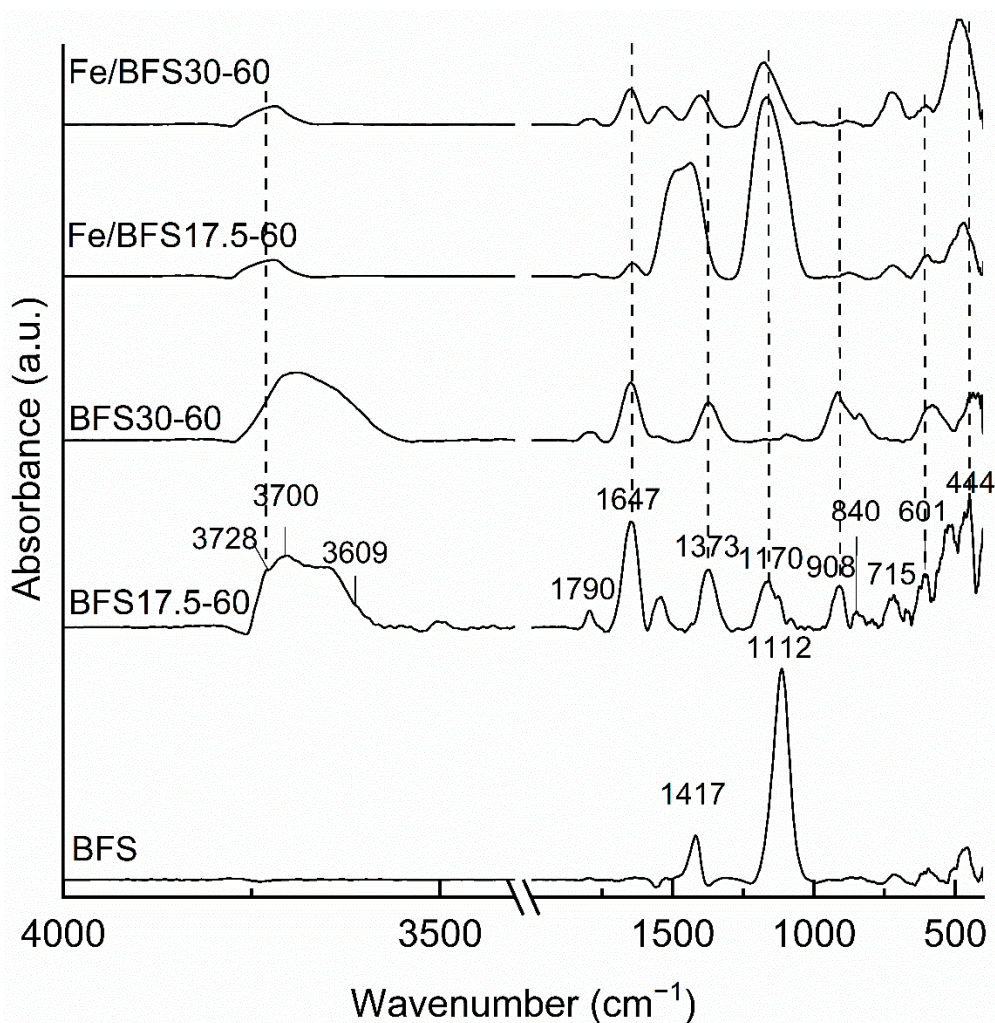


Figure 2. DRIFT spectra of BFS, BFS17.5-60, BFS30-60, Fe/BFS17.5-60, and Fe/BFS30-60 samples.

Alkali-activated samples exhibited several peaks in the analyzed region. The peak at 3730 cm^{-1} for BFS17.5-60 corresponded to silanol groups, which interact with other atoms—for example, in silanol nests [47]—and the absorption peak at $\sim 3700\text{ cm}^{-1}$ revealed the presence of four coordinated Al [48]. Moreover, the band at 3610 cm^{-1} for BFS17.5-60 corresponded to the bridging hydroxyl groups [49]. In the DRIFT spectra of Fe/BFS17.5-60 and Fe/BFS30-60, the peak centers were shifted to higher wavenumbers than those for the samples without iron, probably due to calcination, and the absorption band corresponding to the silanol groups (3730 cm^{-1}) disappeared by the introduction of iron into AAMs [47].

The absorbance bands for BFS17.5-60 and BFS30-60 were observed at 715, 840, 1373, and 1790 cm^{-1} , corresponding to CO_3^{2-} -containing compounds [46]. Bands at 840 and 1790 cm^{-1} connected to Na_2CO_3 , and the band at 715 cm^{-1} corresponded to CaCO_3 [46], while that observed at 1373 cm^{-1} corresponded to hydrotalcite [50], which was also detected in the X-ray diffractograms of these samples (Figure 1). In the DRIFT spectra of Fe/BFS17.5-60 and Fe/BFS30-60, these peaks were slightly shifted to higher wavenumbers, especially for the band corresponding to hydrotalcite, indicative of its decomposition as a result of heat treatment. Furthermore, the peak at $\sim 1650\text{ cm}^{-1}$ observed in all samples corresponded to the H–OH stretching vibrations characteristic of absorbed water [51], the intensity of which slightly decreased due to the heat treatment of iron-containing samples.

All AAMs exhibited several bands corresponding to the Al and Si bonds. The bands at $435\text{--}483\text{ cm}^{-1}$ corresponded to the Si–O–Si and O–Si–O bending vibrations [52], while the absorption peak at $\sim 600\text{ cm}^{-1}$ revealed the presence of Si–O–Si and Al–O–Si symmetric stretching vibrations [53]. The band at $\sim 900\text{ cm}^{-1}$ in the spectra of BFS17.5-60 and BFS30-60

corresponded to the Si–O stretching and Si–OH bending modes [53]. Moreover, the band at $\sim 1170\text{ cm}^{-1}$ corresponded to the Si–O–Si and Al–O–Si asymmetric stretching vibrations [53], and this band was broadened in the spectra of Fe/BFS17.5-60 and Fe/BFS30-60, due to the calcination of these samples [45]. According to [54–56], Fe_2O_3 and Fe_3O_4 species should exhibit IR vibrations at 550 and 780 cm^{-1} and 571 and 590 cm^{-1} , respectively. However, owing to the overlap of the Si and Al vibrations in this wavenumber region, peaks corresponding to Fe cannot be observed in the DRIFT spectra of the prepared samples.

Table 4 lists the concentrations (as wt %) of Ca, Si, Al, Mg, Fe, and Na of BFS17.5-60, BFS30-60, Fe/BFS17.5-60, and Fe/BFS30-60, as determined by ICP-OES analysis.

Table 4. Metal concentrations (as wt %) of selected samples, as determined by ICP-OES analysis.

Sample	Ca	Si	Al (wt %)	Mg	Fe	Na
BFS17.5-60	23.3	14.7	4.34	5.32	0.70	0.24
BFS30-60	21.9	14.4	4.17	5.07	1.86	0.29
Fe/BFS17.5-60	20.3	16.2	4.90	5.77	6.99	0.19
Fe/BFS30-60	20.0	15.1	4.58	5.49	4.95	0.19

The Ca concentrations of the prepared samples were several times lower than those in BFS, while the Si, Al, Mg, and Na concentrations were about the same as those in the raw material (Table 5, experimental). The leaching of Ca probably occurred during the washing of the AAMs using deionized water. BFS contained $\sim 0.5\text{ wt } \%$ iron, and ion exchange led to the increase in the iron concentration to 5–7 wt % for Fe/BFS30-60 and Fe/BFS17.5-60, respectively. The theoretical amount of iron by the employed impregnation method was 5.3 wt %, indicating that ion exchange between BFS17.5-60 and the iron salt is slightly better than that between BFS30-60 and the iron salt.

Table 5. Elemental composition of the blast furnace slag as determined by ICP-OES analysis¹.

	[wt %]											
	Ca	Si	Al	Mg	S	Ti	K	Fe	Na	Mn	Ba	V
BFS	28.70	16.30	5.00	4.87	1.44	0.60	0.58	0.53	0.50	0.28	0.06	0.04

¹ Elements with wt % > 0.01 were reported.

Figure 3 shows the FESEM images of BFS, Fe/BFS17.5-60, and Fe/BFS30-60. AAMs clearly exhibited an irregular, non-crystalline shape (Figure 3b,c). According to EDS analysis, the Al and Mg concentrations were $\sim 5\text{ wt } \%$, while on the Fe catalyst surface, the Si and Ca concentrations were a few percent less than those in the bulk, as determined by ICP-OES (Table 4).

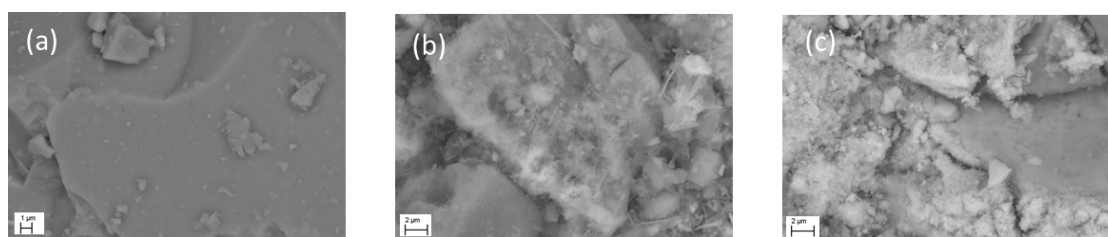


Figure 3. FESEM micrographs of BFS (a), Fe/BFS17.5-60 (b), and Fe/BFS30-60 (c). Dimensions in figures: 1 μm (a) and 2 μm (b,c).

2.3. Oxidation Experiments with AAMs

The prepared AAMs, namely BFS17.5-60, BFS20-60, BFS25-60, and BFS30-60, which were first cured at 60 °C for 24 h, were examined for the CWPO of a BPA aqueous solution. Figure 4 shows the results of these experiments.

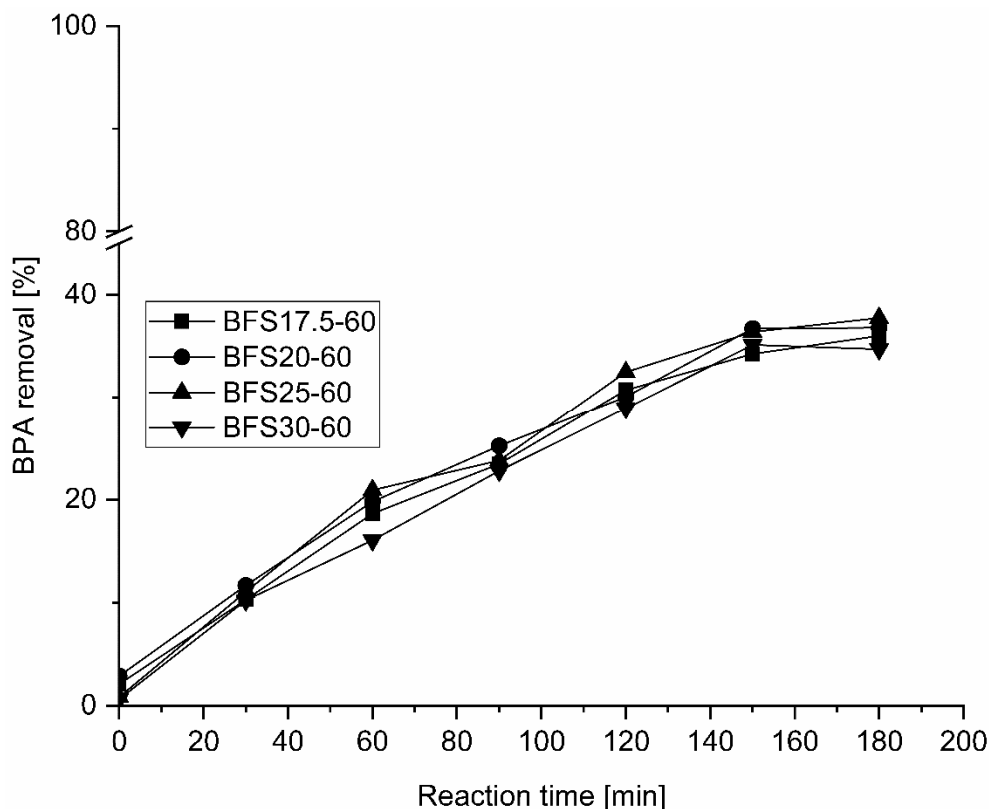


Figure 4. Removal of bisphenol A over AAMs as a function of the reaction time. Reaction conditions: concentration [c], $c[\text{BPA}] = 60 \text{ mg/dm}^3$, $c[\text{H}_2\text{O}_2] = 1.5 \text{ g/dm}^3$, $c[\text{catalyst}] = 4 \text{ g/dm}^3$, temperature [T] = 50 °C, initial pH (6–7).

Oxidation reactions were performed at 50 °C at an initial pH of 6–7, a catalyst concentration of 4 g/dm³, and a H₂O₂ concentration of 1.5 g/dm³. In the absence of a catalyst (not shown), only ~10% of BPA removal was observed, while in the presence of AAMs, BPA removal of 35–39% after 180 min oxidation was observed. Oxidation proceeded during 2.5 h for all samples and stabilized for 3 h. The oxidant H₂O₂ was added in batches; hence, the final addition was performed at 2 h sampling. The total organic carbon (TOC) was measured from the initial and final samples, and 27–31% of organics were removed. The dissolved oxygen (DO) concentration of the BPA samples changed from ~9.5 mg O₂/dm³ to 8.1 mg O₂/dm³ during 180 min oxidation, revealing that at the end of the run, oxygen is still present in the samples. Probably, the used reaction temperature (50 °C) was not sufficiently high for the effective decomposition of H₂O₂ to form active ·OH radicals. In several studies, a higher reaction temperature has been reported to enhance the degradation of H₂O₂, thereby enhancing pollutant removal [57–59].

As all of the AAMs exhibited similar activities for the removal of BPA, samples with the lowest and highest NaOH concentration were selected for further research. Iron was impregnated onto BFS17.5-60 and BFS30-60 samples by ion exchange (Section 3.1), and the prepared Fe catalysts were examined under different reaction conditions.

First, the effect of the addition of the active metal on BFS17.5-60 and BFS30-60 was examined at 50 °C at the initial pH, and a catalyst loading of 4 g/dm³. After 3 h oxidation, BPA removal of 42% and 45% for Fe/BFS17.5-60 and Fe/BFS30-60 were observed, respectively (Figure 5). Using the comparison of BPA removal over AAMs without the active metal (Figure 4), the addition of Fe led to the increased activity of both catalysts, namely

BPA removal of 6% and 10% for BFS17.5-60 and BFS30-60, respectively. TOC removal after 3 h oxidation was at the same level for both catalysts compared to that over the pure supports (30% and 33% for Fe/BFS17.5-60 and Fe/BFS30-60, respectively). During oxidation, the DO concentration decreased slightly from $\sim 9 \text{ mg/O}_2 \text{ dm}^3$ to $6.2\text{--}6.6 \text{ mg/O}_2 \text{ dm}^3$, indicating that hydrogen peroxide is not consumed completely in the runs. Therefore, Fe/BFS17.5-60 and Fe/BFS30-60 were further examined at higher reaction temperatures.

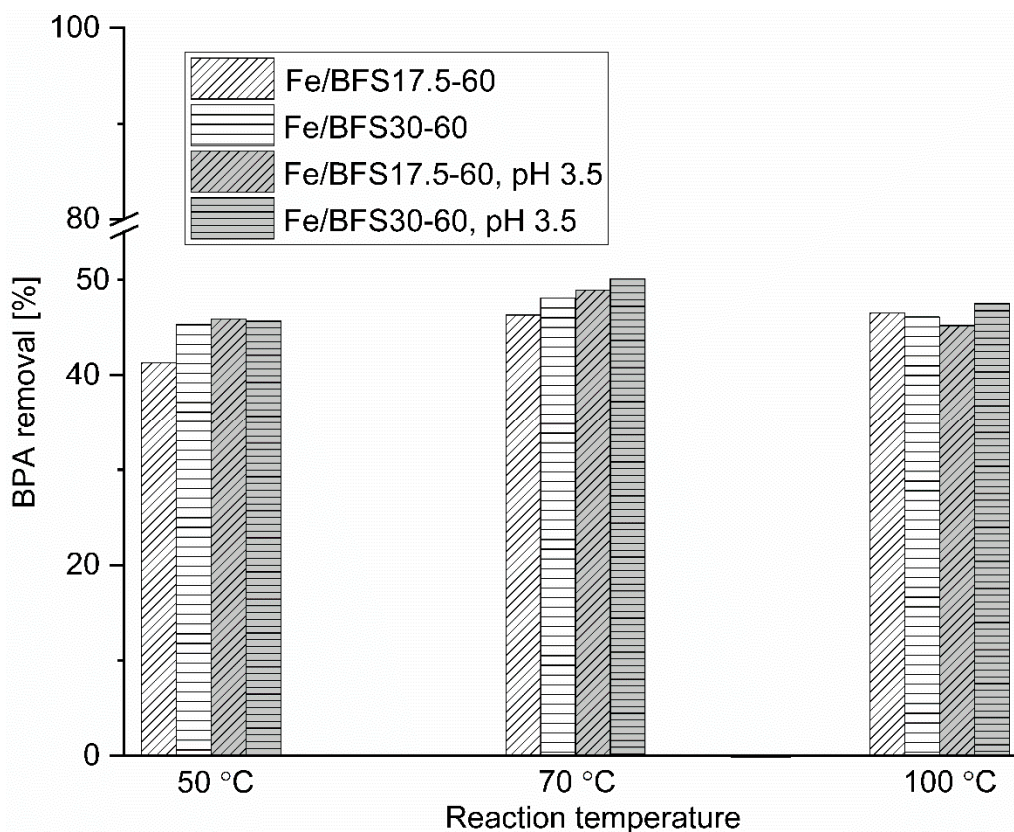


Figure 5. Bisphenol A removal at reaction temperatures of 50 °C, 70 °C, and 100 °C with the Fe/BFS17.5-60 and Fe/BFS30-60 catalysts, at an initial pH of 3.5, a reaction time of 3 h, $[\text{BPA}] = 60 \text{ mg/dm}^3$, $c[\text{H}_2\text{O}_2] = 1.5 \text{ g/dm}^3$, and $c[\text{catalyst}] = 4 \text{ g/dm}^3$.

To investigate the effect of temperature on the CWPO of BPA over Fe/BFS17.5-60 and Fe/BFS30-60, oxidation experiments were performed at 70 °C and 100 °C at the initial pH of the BPA aqueous solution. Typically, with the increase in the reaction temperature, the oxidation rate increases. Furthermore, the decomposition rate of H_2O_2 to active hydroxyl radicals also increases. A higher reaction temperature led to the improved degradation of BPA during 3 h oxidation, with the maximum of 5% over Fe/BFS17.5-60 at 70 °C (Figure 5). The increase in the reaction temperature to 100 °C did not affect BPA removal. During oxidation, the DO concentration decreased from $8.0 \text{ mg/O}_2 \text{ dm}^3$ to $5.7 \text{ mg/O}_2 \text{ dm}^3$ and from $\sim 10.0 \text{ mg/O}_2 \text{ dm}^3$ to $4.2 \text{ mg/O}_2 \text{ dm}^3$ at 70 °C and 100 °C, respectively, revealing that hydrogen peroxide is consumed in the reaction. However, owing to the low degradation level of BPA at 100 °C, hydrogen peroxide was probably decomposed directly to H_2O without the formation of hydroxyl radicals.

Typically, homogeneous iron catalysts for CWPO (Fenton process) are used at a pH of ~ 3 , which is known to be optimum for the decomposition of organic compounds [60]. The effect of pH on the degradation level of BPA was investigated at pH 3.5, in addition to the initial pH (6–7) by using Fe/BFS17.5-60 and Fe/BFS30-60 catalysts. The effect of pH was examined at 50 °C, 70 °C, and 100 °C. The pH of the BPA solution was adjusted to 3.5 using 2.0 M HNO_3 before oxidation. At 50 °C and pH 3.5, BPA removal increased by 5% over Fe/BFS17.5-60, while over Fe/BFS30-60, it was almost the same after 3 h

oxidation compared to experiments performed at the initial pH of BPA (Figure 5). The DO concentration of the liquid samples was considerably higher (at the end of the run for Fe/BFS17.5-60, 14 mg/O₂ dm³) than that after oxidation at the initial pH. Therefore, acidic pH promotes the formation of hydroxyl radicals during the reaction. However, Fe catalysts did not exhibit considerably higher activity for BPA removal than that at the initial pH, probably due to the basic surfaces of Fe/BFS17.5-60 and Fe/BFS30-60.

At pH 3.5 and 70 °C (Figure 5), the DO concentration was the same during tests compared to that in experiments at the initial pH, and the pH change of the BPA solution led to an increase in BPA removal by only 3% and 2% over Fe/BFS17.5-60 and Fe/BFS30-60, respectively. At 100 °C and pH 3.5, BPA removal after 3 h was around the same for both Fe catalysts compared with that observed at 100 °C and at the initial pH. However, notably, owing to the basicity of Fe catalysts, the pH of the BPA solution changed to basic during runs in all experiments. The decomposition of H₂O₂ to ·OH radicals is the key step in CWPO. However, under a basic reaction pH, the generation of hydroxyl radicals was restricted, thereby further decreasing the degradation of BPA [61]. Thus, the change in pH marginally affects BPA removal.

The adsorption capacity of the Fe catalysts was examined under the severest reaction conditions in this study, i.e., pH of 3.5, a reaction temperature of 100 °C, in the absence of the oxidant, and a catalyst concentration of 4 g/dm³. For Fe/BFS17.5-60 and Fe/BFS30-60, during the 3 h experiment, 12% and 17% of BPA was adsorbed, respectively, revealing that Fe/BFS17.5-60 is catalytically more active than Fe/BFS30-60. The higher adsorption capacity of Fe/BFS30-60 was related to the higher specific surface area of this sample (Table 3).

2.4. Stability of the Used Catalysts

The possible leaching of the elements from the prepared AAMs was examined by ICP-OES in detail, in addition to the leaching tests (Section 2.1) after oxidation. The oxidized water samples were immediately filtered after 3 h CWPO using a 0.45 µm cellulose nitrate filter to remove the solid catalysts. The Al, Si, and Ca concentrations were determined from the oxidized water samples catalyzed by BFS17.5-60, BFS20-60, BFS25-60, and BFS30-60, and in addition to these elements, Fe was analyzed from the filtered samples catalyzed by Fe/BFS17.5-60 and Fe/BFS30-60. According to the results, the leaching of Ca and Si was observed under all of the utilized reaction conditions with all catalysts. In all of the oxidized water samples, the Ca concentration was 25–50 mg/dm³, and the Si concentration was 11–19 mg/dm³. However, notably, the Ca concentration was slightly lower in the water samples catalyzed by AAMs without iron. Therefore, the heat treatment of Fe catalysts (Section 3.1) led to the increased dissolution of Ca in the water phase during oxidation treatment. The leaching of Ca was around the same level as that detected in stability tests (Section 2.1) with BFS17.5-60, BFS20-60, BFS25-60, and BFS30-60, revealing that these samples also can be used at reaction temperatures > 100 °C and pressures ≥ 2 MPa.

The Al concentration of aqueous BPA samples oxidized at the initial pH was 1.0–1.4 mg/dm³. The dissolution of Al was slightly higher at 150 °C and 2.0 MPa (Table 1), i.e., under conditions of the stability test, than that under CWPO reaction conditions. However, in the case of oxidation experiments performed at a pH of 3.5, and at temperatures 50 °C, 70 °C, and 100 °C over that of Fe/BFS17.5-60 and Fe/BFS30-60, 0.6–1.2 mg/dm³ of Al was leached from the catalysts in the obtained effluents. Therefore, the dissolution of Al from the prepared AAMs is more dominant in the CWPO of BPA, which is conducted at the initial pH. Onisei et al. [41] have investigated the leaching behavior of several elements (e.g., Si, Pb, Ca, Zn, Al) from fly ash-based geopolymers. The study was performed in the pH range of 6–13. According to their results, the leaching of Al increased slightly in the pH range of 10.5–13.0. In the CWPO of BPA, the initial pH of the BPA solution was 6–7. However, at the end of the run, the effluent pH was ~11, due to the basic character of the Fe catalysts. Moreover, in CWPO experiments, which were started at a pH of 3.5, the pH of the BPA solution was ~10 in the oxidized water sample. Therefore, the adjustment of

the pH at the start of the CWPO of BPA did not considerably affect the removal of BPA, but it decreased the leaching of Al from the Fe catalysts.

However, the leaching of Ca, Si, and Al was not related to the removal of BPA, because those elements were not active in CWPO. The stability of the material is a key characteristic of the catalyst; therefore, the preparation method of AAM-based catalysts should be carefully considered. Moreover, the leaching of iron was rather negligible (maximum of 0.2 mg/dm^3 at $70 \text{ }^\circ\text{C}$ and at the initial pH) using Fe/BFS17.5-60 and Fe/BFS30-60 at the employed reaction temperatures and pH. Therefore, the CWPO of BPA with these catalysts proceeded via a heterogeneous reaction.

The activity and durability in consecutive tests and the effect of heat treatment as a regeneration method were examined using Fe/BFS7.5-60 at $50 \text{ }^\circ\text{C}$, at the initial pH, and at H_2O_2 and catalyst concentrations of 1.5 g/dm^3 and 4.0 g/dm^3 , respectively. To have sufficient material for consecutive tests and regeneration, 12 runs were performed in total, and the catalysts used in these experiments were collected and combined. Between consecutive experiments, the used catalyst was filtered from the effluent and dried at $105 \text{ }^\circ\text{C}$ for the subsequent runs.

After the first oxidation reaction, BPA removal of 41% was observed, which decreased to ~6% after the second run using the same catalyst (Figure 6). Furthermore, BPA removal after the third experiment, which used Fe/BFS17.5-60 twice, was practically the same (34%) as that observed in the second run, indicative of the catalyst's stability for multiple cycles in the CWPO of BPA. However, the removal of BPA after three cycles using Fe/BFS17.5-60 was around the same as that using BFS17.5-60 for one cycle, revealing that the addition of Fe does not significantly affect catalytic activity due to the basic reaction pH. Moreover, TOC results confirmed the reusability of Fe/BFS17.5-60, while BPA removal was the same during the three consecutive tests.

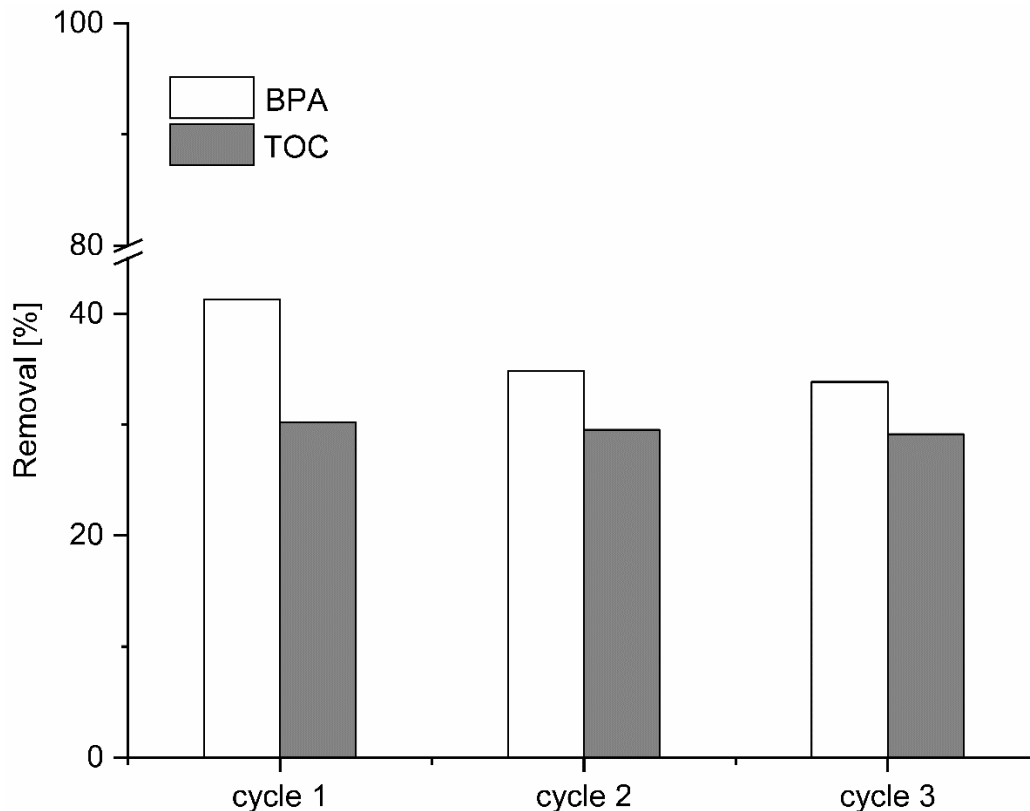


Figure 6. Consecutive tests using Fe/BFS17.5-60 for the CWPO of BPA. Reaction conditions: $c[\text{BPA}] = 60 \text{ mg/dm}^3$, $c[\text{H}_2\text{O}_2] = 1.5 \text{ g/dm}^3$, $c[\text{catalyst}] = 4 \text{ g/dm}^3$, $T = 50 \text{ }^\circ\text{C}$, initial pH (6–7).

The regeneration of once-used Fe/BFS17.5-60 was examined by heat treatment at 250 °C and 500 °C. The procedure was performed by increasing the temperature at a rate of 1 °C/min to the reaction temperature, at which the catalyst was kept for 2 h. After oxidation, 34% and 32% BPA removal was observed at 250 °C and 500 °C, respectively, using Fe/BFS17.5-60. Therefore, the regeneration procedure is not effective at returning the activity of the catalysts to the original level. In addition, carbon deposition is confirmed to not be responsible for the activity decrease of Fe/BFS17.5-60, because heat treatment at elevated temperatures is a typical regeneration procedure for catalysts with carbon deactivation [62].

2.5. Characterization of the Used Catalysts

Figure 7 shows the X-ray diffractograms of BFS17.5-60, BFS30-60, Fe/BFS17.5-60, and Fe/BFS30-60 after oxidation at the initial pH and at a reaction temperature of 50 °C. According to XRD analysis, the hydrotalcite phase (denoted by #, ICDD file 00-022-0700) was still present in BFS17.5-60 and BFS30-60, and the CaCO₃ phase (α , ICDD file 01-083-4609) was observed in all samples. Moreover, in the X-ray diffractograms of Fe/BFS17.5-60 and Fe/BFS30-60, the Fe₃O₄ and Fe₂O₃ iron phases (denoted by +: ICDD file 04-008-8146 and *: ICDD file 04-015-7029, respectively) were still present, but the high Ca concentration of samples led to the overlap of the CaCO₃ peaks with those of Fe₃O₄ and Fe₂O₃ at 2 θ of 36° and Fe₃O₄ at 2 θ of 43°.

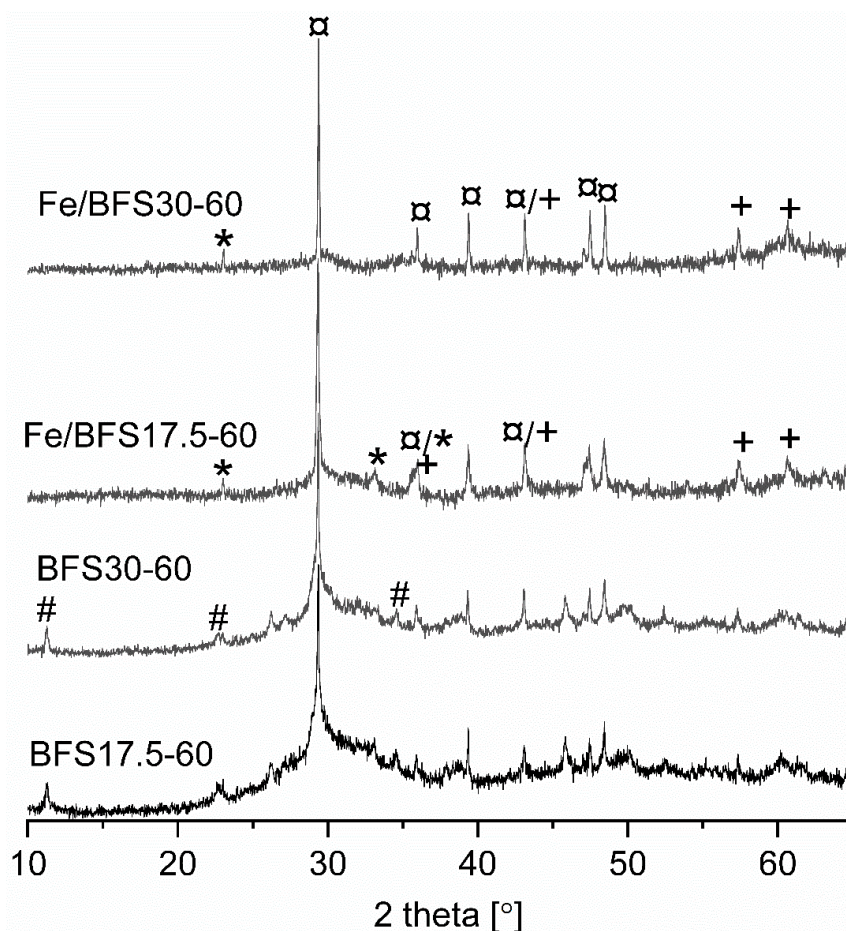


Figure 7. X-ray diffractograms of used BFS17.5-60, BFS30-60, Fe/BFS17.5-60, and Fe/BFS30-60. (#) ICDD file 00-022-0700 (Mg₆Al₂CO₃(OH)₁₆·4H₂O, hydrotalcite); (α) ICDD file 01-083-4609 (CaCO₃); (*) ICDD file 04-015-7029 (Fe₂O₃); (+) ICDD file 04-008-8146 (Fe₃O₄).

Furthermore, acidic pH and a higher reaction temperature did not affect the phase structure, and hydrotalcite was still observed in the X-ray diffractograms of BFS30-60 and BFS17.5-60 (results not shown).

The specific surface area of samples was analyzed after the oxidation of BPA at the initial pH and at reaction temperatures of 50 °C for BFS17.5-60 and BFS30-60, as well as reaction temperatures of 50 °C and 70 °C for Fe/BFS17.5-60 and Fe/BFS30-60. The BET results for used BFS17.5-60 and BFS30-60 revealed that the specific surface areas were 10.4 and 18.5 m²/g, respectively, revealing that the surface area of BFS30-60 decreases to ~30%, while a rather negligible change in the surface area of BFS17.5-60 was observed (Table 3). For Fe catalysts, the specific surface areas increased after oxidation. In case of Fe/BFS17.5-60, the surface area was ~45% higher, and in case of Fe/BFS30-60, it doubled compared to that of the fresh catalyst (Table 3). Clearly, during oxidation, the Fe catalyst surface is refined by H₂O₂. For example, Han et al. [63] and Liu et al. [64] have used hydrogen peroxide to modify surface properties, i.e., to increase the surface area and porosity of materials. However, the larger specific surface area did not improve the removal of BPA in consecutive tests using Fe/BFS17.5-60 (Figure 6); therefore, the CWPO of BPA is not a surface area-specific reaction, as is the case for the catalytic wet air oxidation of BPA [65].

3. Materials and Methods

In this section, the preparation method and characterization techniques of catalysts are described. In addition, reaction conditions for the CWPO of the bisphenol A aqueous solution are presented.

3.1. Preparation of Alkali-Activated Materials and Fe Catalysts

AAMs were synthesized using powdered blast furnace slag (BFS) obtained from the Finnish steel industry. Table 5 lists the elemental composition of the slag, as determined by ICP-OES analysis.

AAMs were prepared by mixing 40 g of BFS with 17.5, 20.0, 25.0, and 30.0 g of 50 wt % sodium hydroxide (NaOH ≥ 97%, Merck, Darmstadt, Germany). The formed pastes were poured into molds, followed by consolidation in plastic bags at room temperature for 168 h. For comparison, consolidation was first performed at 60 °C for 24 h and then for 144 h at room temperature. The prepared samples were named according to their NaOH concentration and consolidation temperature (Table 6). Before use, the materials were crushed using a jaw crusher, sieved to a particle size of 0.5–2.0 mm, and washed with de-ionized water. As the active metal, Fe was impregnated on the AAMs by ion exchange. First, 5 g of AAM and 0.5 dm³ of 0.01 M (NH₄)₂Fe(SO₄)₂ (99.0–101.5%, Merck, Darmstadt, Germany) were mixed in a sand bath and left overnight at 80 °C. The solids were collected by filtration, washed with deionized water, and dried overnight at 120 °C. Finally, the prepared Fe catalysts were subjected to calcination at 500 °C for 2 h, increasing the temperature from room temperature to the target temperature at a rate of 1 °C/min.

Table 6. Abbreviations of the prepared AAMs and Fe catalysts. Samples were named according to their NaOH concentrations and curing temperatures.

Studied Samples	50 wt % NaOH [g]	Consolidation T [°C]	Si/Na Ratio
BFS17.5-20	17.5	20	3.24
BFS17.5-60	17.5	60	3.24
BFS20-20	20.0	20	2.84
BFS20-60	20.0	60	2.84
BFS25-20	25.0	20	2.27
BFS25-60	25.0	60	2.27
BFS30-20	30.0	20	1.89
BFS30-60	30.0	60	1.89
Fe/BFS17.5-60	17.0	60	3.24
Fe/BFS30-60	30.0	60	2.84

3.2. Stability of AAMs

The stability of as-prepared AAMs was examined by measuring the possible leaching of the main elements of samples (i.e., Al, Ca, Mg, Na, and Si) to the water phase. Before the test, samples were crushed using a jaw crusher, sieved to a particle size of 1–2 mm, washed with deionized water, and dried. Stability tests were performed in a pressurized reactor at 150 °C and under a nitrogen atmosphere of 2 MPa. The crushed AAMs at a concentration of 4 g/dm³ were continuously stirred for 4 h with 0.16 dm³ of deionized water. The ready leaching of elements was detected by conductivity measurement during and after the test, while the possible dissolution of Al, Ca, Mg, Na, and Si was analyzed by inductively coupled plasma–optical emission spectroscopy (ICP-OES, Thermo Electron iCAP 6500 Duo, Thermo Fisher Scientific, Waltham, MA, USA).

3.3. Characterization of Samples

The surface morphology and chemical composition of the prepared AAMs were analyzed by field emission scanning electron microscopy (FESEM; Carl Zeiss Microscopy GmbH, Jena, Germany) combined with energy-dispersive X-ray spectroscopy (EDS; analyzer at the Centre for Material Analysis, University of Oulu, Finland). The phase composition of AAMs was determined by powder X-ray diffraction (XRD) with a PANalytical X'Pert Pro X-ray diffractometer (Malvern PANalytical, Almelo, The Netherlands). XRD analysis was performed by scanning two theta values between 10° and 70° with monochromatic Cu K α 1 ($\lambda = 1.5406 \text{ \AA}$) at 45 kV and 40 mA at a scan speed of 0.021 °/s. Crystalline phases were identified by HighScore Plus software using the Powder Diffraction File standards from the International Centre for Diffraction DATA ICDD (PDF-4+ 2020 RDB). Diffuse-reflectance infrared Fourier transform spectroscopy (DRIFTS) was employed to investigate the degree of polymerization of the prepared samples. DRIFT spectra were recorded on a Bruker PMA 50 Vertex 80 V (Bruker, Billerica, MA, USA), equipped with a Harrick Praying Mantis diffuse reflection accessory and a high-temperature reaction chamber, by baseline measurement using KBr. Before analysis, the sample chamber was flushed with nitrogen (100 cm³/min), heated at a rate of 10 °C/min to the target temperature of 120 °C, and maintained at that temperature for 30 min. Measurements were conducted at 400–4000 cm^{−1} with a resolution of 4 cm^{−1} and 500 scans per minute. The specific surface areas and porosity were obtained from nitrogen adsorption–desorption isotherms at the liquid nitrogen temperature (−196 °C) by the Brunauer–Emmett–Teller (BET) method on a Micromeritics ASAP 2020 system (Micromeritics Instrument Corporation, Norcross, GA, USA). The pore size distribution was calculated by density functional theory (DFT) [66]. Furthermore, the main elements of the prepared samples (Al, Ca, Mg, Na, and Si) and the active metal Fe were analyzed by ICP-OES analysis (Thermo Electron iCAP 6500 Duo, Thermo Fisher Scientific, Waltham, MA, USA).

3.4. Catalytic Wet Peroxide Oxidation Experiments

Oxidation experiments with a BPA aqueous solution (60 mg/L) were performed in a three-necked flask equipped with a reflux condenser. BFS30-60, BFS25-60, BFS20-60, BFS17.5-60, Fe/BFS30-60, and Fe/BFS17.5-60 were examined at a reaction temperature of 50 °C, a H₂O₂ concentration of 1.5 g/dm³ (stoichiometric amount to total oxidation of BPA), and a catalyst loading of 4 g/dm³, with a reaction volume of 0.16 dm³. Oxidation was started while the reaction temperature was reached by the addition of H₂O₂, which was added in batches to maintain a stable oxidation agent concentration during the 3 h test. Water samples were taken as a function of reaction time, which were filtered using a 0.45 μm filter paper. The pH and dissolved oxygen (DO) were measured from water samples during the experiment. Furthermore, the effects of pH and temperature on oxidation were examined using Fe/BFS30-60 and Fe/BFS17.5-60. For evaluating the stability and reusability of the prepared materials, Fe/BFS17.5-60 was examined in three consecutive oxidation reactions. In addition, the regeneration of used Fe/BFS17.5-60 was

performed by heating the catalyst for 2 h at two temperatures (i.e., 250 °C and 500 °C) to examine the effect of heat treatment on the activity of the used catalyst.

3.5. Water Sample Analysis

The BPA concentration of the water samples was determined by high-pressure liquid chromatography (HPLC) equipped with a Waters 996 photodiode array (PDA) detector (Waters Corp., Milford, MA, USA) at a wavelength of 226 nm. A mixture of 0.1% trifluoroacetic acid (TFA) in methanol and 0.1% TFA in water at a flow rate of 0.4 cm³/min was used as the eluent mixture to separate compounds on a SunFire™ C18 5-μm 2.1 × 100 mm column (Waters Corp., Milford, MA, USA) operated at 30 °C. The total organic carbon (TOC) concentration of water samples was determined from the initial and final samples on a Skalar FormacsHT Total Organic Carbon/total nitrogen analyzer (Breda, The Netherlands). Possible leaching of Al, Ca, Mg, Na, and Si was analyzed from the final samples after oxidation by ICP-OES analysis (Thermo Electron iCAP 6500 Duo, Thermo Fisher Scientific, Waltham, MA, USA).

4. Conclusions

In this study, novel, eco-efficient, BFS-based alkali-activated materials were prepared and examined as catalysts for the CWPO of a BPA aqueous solution. AAMs consolidated at 60 °C were selected for catalytic studies, as they were more stable in the aqueous phase, and the phase structure was more porous than that of the samples cured at room temperature. BFSXX-60 samples exhibited moderate activity for the CWPO of BPA at 50 °C and at the initial pH. The catalytic activities of Fe/BFS17.5-60 and Fe/BFS30-60 were examined at reaction temperatures of 50 °C, 70 °C, and 100 °C, and at the initial pH and a pH of 3.5. The addition of iron to the BFS-based materials led to the increased removal of BPA, with the highest BPA removal (50%) achieved using Fe/BFS30-60 at a pH of 3.5 at 70 °C. Furthermore, Fe/BFS17.5-60 exhibited moderate activity, even after three consecutive tests, and no change in the phase structure of the AAMS after the oxidation reaction was observed. Although prepared AAMs are interesting alternatives for catalytic water-phase applications, dissolution of Ca and Si, as well as small amounts of Al, was observed from AAMs during oxidation. In addition, the basic character of the material prevented higher removal of BPA. Therefore, additional attention should be focused on the stability and surface pH (e.g., pretreatment with acid) of AAMs in our future studies.

Author Contributions: Methodology, A.H. and J.P.; software, A.H.; investigation, A.H. and T.H.; data curation, A.H.; writing—original draft preparation, A.H.; writing—review and editing, all authors; visualization, A.H.; project administration, U.L.; funding acquisition, U.L. and A.H. All authors have read and agreed to the published version of the manuscript.

Funding: This work was partly funded by the Renlund Foundation, within the project “New catalyst materials for wastewater treatment from industrial side streams”.

Data Availability Statement: The data presented in this study are available within the article (tables and figures). The data presented in this study are available on request from the corresponding author.

Acknowledgments: Financial support from Renlund Foundation is gratefully acknowledged. Henrik Romar, Katariina Hautamäki, Tiina Leskelä, Ilkka Vesavaara, Jere Taipalus, Eemeli Koskela, Santeri Impiö, and Carlos Gonzales are acknowledged.

Conflicts of Interest: The authors declare no conflict of interest. The funders had no role in the design of the study; in the collection, analyses, or interpretation of data; in the writing of the manuscript, or in the decision to publish the results.

Abbreviations

AAM	Alkali-activated material
AOP	Advanced oxidation process
BET	Brunauer–Emmett–Teller
BFS	Blast furnace slag
BPA	Bisphenol A
CWPO	Catalytic wet peroxide oxidation
DFT	Density functional theory
DO	Dissolved oxygen
DRIFTS	Diffuse-reflectance infrared Fourier transform spectroscopy
Fe/BFS30-60	Iron-containing blast furnace slag-based catalyst
FESEM-EDS	Field emission scanning electron microscope with energy-dispersive X-ray spectroscopy
FTIR	Fourier transform infrared spectroscopy
HPLC	High-pressure liquid chromatography
ICDD	International Centre for Diffraction Data
ICP-OES	Inductively coupled plasma-optical emission spectroscopy
IR	Infrared
PDA	Photodiode array
PV	Pore volume
SSA	Specific surface areas
TFA	Trifluoroacetic acid
TOC	Total organic carbon
UV	Ultraviolet
XRD	X-ray diffraction

References

- Provis, J.L.; Van Deventer, J.S.J. 1—Introduction to geopolymers. *Geopolymers* **2009**, 1–11. [[CrossRef](#)]
- Bernal, S.A.; Provis, J.L.; Fernández-Jiménez, A.; Krivenko, P.V.; Kavalerova, E.; Palacios, M.; Shi, C. Binder Chemistry—High-Calcium Alkali-Activated Materials. In *Alkali Activated Materials: State-of-the-Art Report, RILEM TC 224-AAM*; Provis, J.L., van Deventer, J.S.J., Eds.; Springer: Dordrecht, The Netherlands, 2014; pp. 59–91.
- Duxson, P.; Fernández-Jiménez, A.; Provis, J.L.; Lukey, G.C.; Palomo, A.; van Deventer, J.S.J. Geopolymer technology: The current state of the art. *J. Mater. Sci.* **2007**, *42*, 2917–2933. [[CrossRef](#)]
- Davidovits, J. Geopolymers. *J. Therm. Anal.* **1991**, *37*, 1633–1656. [[CrossRef](#)]
- Medpelli, D.; Seo, J.; Seo, D. Geopolymer with Hierarchically Meso-/Macroporous Structures from Reactive Emulsion Templating. *J. Am. Ceram. Soc.* **2014**, *97*, 70–73. [[CrossRef](#)]
- Luukkonen, T.; Sarkkinen, M.; Kemppainen, K.; Rämö, J.; Lassi, U. Metakaolin geopolymer characterization and application for ammonium removal from model solutions and landfill leachate. *Appl. Clay Sci.* **2016**, *119*, 266–276. [[CrossRef](#)]
- Luukkonen, T.; Runtti, H.; Niskanen, M.; Tolonen, E.; Sarkkinen, M.; Kemppainen, K.; Rämö, J.; Lassi, U. Simultaneous removal of Ni(II), As(III), and Sb(III) from spiked mine effluent with metakaolin and blast-furnace-slag geopolymers. *J. Environ. Manag.* **2016**, *166*, 579–588. [[CrossRef](#)]
- Khan, M.I.; Min, T.K.; Azizli, K.; Sufian, S.; Ullah, H.; Man, Z. Effective removal of methylene blue from water using phosphoric acid based geopolymers: Synthesis, characterizations and adsorption studies. *RSC Adv.* **2015**, *5*, 61410–61420. [[CrossRef](#)]
- Yousef, R.I.; El-Eswed, B.; Alshaaer, M.; Khalili, F.; Houry, H. The influence of using Jordanian natural zeolite on the adsorption, physical, and mechanical properties of geopolymers products. *J. Hazard. Mater.* **2009**, *165*, 379–387. [[CrossRef](#)]
- Sazama, P.; Bortnovsky, O.; Dědeček, J.; Tvarůžková, Z.; Sobalík, Z. Geopolymer based catalysts—New group of catalytic materials. *Catal. Today* **2011**, *164*, 92–99. [[CrossRef](#)]
- Mejía de Gutiérrez, R.; Villaquirán-Caicedo, M.A.; Guzmán-Aponte, L.A. Alkali-activated metakaolin mortars using glass waste as fine aggregate: Mechanical and photocatalytic properties. *Constr. Build. Mater.* **2020**, *235*, 117510. [[CrossRef](#)]
- Kang, L.; Zhang, Y.J.; Zhang, L.; Zhang, K. Preparation, characterization and photocatalytic activity of novel CeO₂ loaded porous alkali-activated steel slag-based binding material. *Int. J. Hydrog. Energy* **2017**, *42*, 17341–17349. [[CrossRef](#)]
- Sharma, S.; Medpelli, D.; Chen, S.; Seo, D. Calcium-modified hierarchically porous aluminosilicate geopolymer as a highly efficient regenerable catalyst for biodiesel production. *RSC Adv.* **2015**, *5*, 65454–65461. [[CrossRef](#)]
- Guerra, P.; Kim, M.; Teslic, S.; Alae, M.; Smyth, S.A. Bisphenol-A removal in various wastewater treatment processes: Operational conditions, mass balance, and optimization. *J. Environ. Manag.* **2015**, *152*, 192–200. [[CrossRef](#)] [[PubMed](#)]
- Kitamura, S.; Suzuki, T.; Sanoh, S.; Kohta, R.; Jinno, N.; Sugihara, K.; Yoshihara, S.; Fujimoto, N.; Watanabe, H.; Ohta, S. Comparative Study of the Endocrine-Disrupting Activity of Bisphenol A and 19 Related Compounds. *Toxicol. Sci.* **2005**, *84*, 249–259. [[CrossRef](#)] [[PubMed](#)]

16. Melcer, H.; Klečka, G. Treatment of Wastewaters Containing Bisphenol A: State of the Science Review. *Water Environ. Res.* **2011**, *83*, 650–666. [[CrossRef](#)] [[PubMed](#)]
17. Chen, J.; Huang, X.; Lee, D. Bisphenol A removal by a membrane bioreactor. *Process. Biochem.* **2008**, *43*, 451–456. [[CrossRef](#)]
18. Shabtai, I.A.; Mishaal, Y.G. Polycyclodextrin–Clay Composites: Regenerable Dual-Site Sorbents for Bisphenol A Removal from Treated Wastewater. *ACS Appl. Mater. Interfaces* **2018**, *10*, 27088–27097. [[CrossRef](#)] [[PubMed](#)]
19. Juhola, R.; Heponiemi, A.; Tuomikoski, S.; Hu, T.; Vielma, T.; Lassi, U. Preparation of Novel Fe Catalysts from Industrial By-Products: Catalytic Wet Peroxide Oxidation of Bisphenol A. *Top. Catal.* **2017**, *60*, 1387–1400. [[CrossRef](#)]
20. Salimi, M.; Esrafil, A.; Gholami, M.; Jonidi Jafari, A.; Rezaei Kalantary, R.; Farzadkia, M.; Kermani, M.; Sobhi, H.R. Contaminants of emerging concern: A review of new approach in AOP technologies. *Environ. Monit. Assess.* **2017**, *189*, 414. [[CrossRef](#)]
21. Kovačič, A.; Česen, M.; Laimou-Geraniou, M.; Lambropoulou, D.; Kosjek, T.; Heath, D.; Heath, E. Stability, biological treatment and UV photolysis of 18 bisphenols under laboratory conditions. *Environ. Res.* **2019**, *179*, 108738. [[CrossRef](#)]
22. Umar, M.; Roddick, F.; Fan, L.; Aziz, H.A. Application of ozone for the removal of bisphenol A from water and wastewater—A review. *Chemosphere* **2013**, *90*, 2197–2207. [[CrossRef](#)] [[PubMed](#)]
23. Sharma, J.; Mishra, I.M.; Kumar, V. Degradation and mineralization of Bisphenol A (BPA) in aqueous solution using advanced oxidation processes: UV/H₂O₂ and UV/S₂O₈²⁻—oxidation systems. *J. Environ. Manag.* **2015**, *156*, 266–275. [[CrossRef](#)] [[PubMed](#)]
24. Dudziak, M.; Burdzik, E. Oxidation of bisphenol A from simulated and real urban wastewater effluents by UV, O₃ and UV/O₃. *Null* **2016**, *57*, 1075–1083. [[CrossRef](#)]
25. Jia, C.; Wang, Y.; Zhang, C.; Qin, Q.; Kong, S.; Kouakou Yao, S. Photocatalytic Degradation of Bisphenol A in Aqueous Suspensions of Titanium Dioxide. *Environ. Eng. Sci.* **2012**, *29*, 630–637. [[CrossRef](#)]
26. Ahmadi, M.; Rahmani, H.; Takdastan, A.; Jaafarzadeh, N.; Mostoufi, A. A novel catalytic process for degradation of bisphenol A from aqueous solutions: A synergistic effect of nano-Fe₃O₄@Al₂O₃-Fe on O₃/H₂O₂. *Process. Saf. Environ. Prot.* **2016**, *104*, 413–421. [[CrossRef](#)]
27. Perathoner, S.; Centi, G. Wet hydrogen peroxide catalytic oxidation (WHPCO) of organic waste in agro-food and industrial streams. *Top. Catal.* **2005**, *33*, 207–224. [[CrossRef](#)]
28. Tu, Y.; Tian, S.; Kong, L.; Xiong, Y. Co-catalytic effect of sewage sludge-derived char as the support of Fenton-like catalyst. *Chem. Eng. J.* **2012**, *185–186*, 44–51. [[CrossRef](#)]
29. Messele, S.A.; Soares, O.S.G.P.; Órfão, J.J.M.; Stüber, F.; Bengoa, C.; Fortuny, A.; Fabregat, A.; Font, J. Zero-valent iron supported on nitrogen-containing activated carbon for catalytic wet peroxide oxidation of phenol. *Appl. Catal. B Environ.* **2014**, *154–155*, 329–338. [[CrossRef](#)]
30. Dehkordi, A.M.; Ebrahimi, A.A. Catalytic Wet Peroxide Oxidation of Phenol in a New Two-Impinging-Jets Reactor. *Ind. Eng. Chem. Res.* **2009**, *48*, 10619–10626. [[CrossRef](#)]
31. Domínguez, C.M.; Ocón, P.; Quintanilla, A.; Casas, J.A.; Rodriguez, J.J. Graphite and carbon black materials as catalysts for wet peroxide oxidation. *Appl. Catal. B Environ.* **2014**, *144*, 599–606. [[CrossRef](#)]
32. Martín-Martínez, M.; Machado, B.F.; Serp, P.; Morales-Torres, S.; Silva, A.M.T.; Figueiredo, J.L.; Faria, J.L.; Gomes, H.T. Carbon nanotubes as catalysts for wet peroxide oxidation: The effect of surface chemistry. *Catal. Today* **2020**, *357*, 332–340. [[CrossRef](#)]
33. Juhola, R.; Heponiemi, A.; Tuomikoski, S.; Hu, T.; Prokkola, H.; Romar, H.; Lassi, U. Biomass-based composite catalysts for catalytic wet peroxide oxidation of bisphenol A: Preparation and characterization studies. *J. Environ. Chem. Eng.* **2019**, *7*, 103127. [[CrossRef](#)]
34. Yan, Y.; Jiang, S.; Zhang, H.; Zhang, X. Preparation of novel Fe-ZSM-5 zeolite membrane catalysts for catalytic wet peroxide oxidation of phenol in a membrane reactor. *Chem. Eng. J.* **2015**, *259*, 243–251. [[CrossRef](#)]
35. Valkaj, K.M.; Katovič, A.; Zrnčević, S. Catalytic Properties of Cu/13X Zeolite Based Catalyst in Catalytic Wet Peroxide Oxidation of Phenol. *Ind. Eng. Chem. Res.* **2011**, *50*, 4390–4397. [[CrossRef](#)]
36. Galeano, L.A.; Gil, A.; Vicente, M.A. Effect of the atomic active metal ratio in Al/Fe-, Al/Cu- and Al/(Fe–Cu)-intercalating solutions on the physicochemical properties and catalytic activity of pillared clays in the CWPO of methyl orange. *Appl. Catal. B Environ.* **2010**, *100*, 271–281. [[CrossRef](#)]
37. Garrido-Ramirez, E.G.; Sivaiah, M.V.; Barrault, J.; Valange, S.; Theng, B.K.G.; Ureta-Zañartu, M.S.; Mora, M.d.I.L. Catalytic wet peroxide oxidation of phenol over iron or copper oxide-supported allophane clay materials: Influence of catalyst SiO₂/Al₂O₃ ratio. *Microporous Mesoporous Mater.* **2012**, *162*, 189–198. [[CrossRef](#)]
38. Li, C.; He, Y.; Tang, Q.; Wang, K.; Cui, X. Study of the preparation of CdS on the surface of geopolymer spheres and photocatalyst performance. *Mater. Chem. Phys.* **2016**, *178*, 204–210. [[CrossRef](#)]
39. Fallah, M.; MacKenzie, K.J.D.; Hanna, J.V.; Page, S.J. Novel photoactive inorganic polymer composites of inorganic polymers with copper(I) oxide nanoparticles. *J. Mater. Sci.* **2015**, *50*, 7374–7383. [[CrossRef](#)]
40. Falah, M.; MacKenzie, K.J.D.; Knibbe, R.; Page, S.J.; Hanna, J.V. New composites of nanoparticle Cu (I) oxide and titania in a novel inorganic polymer (geopolymer) matrix for destruction of dyes and hazardous organic pollutants. *J. Hazard. Mater.* **2016**, *318*, 772–782. [[CrossRef](#)]
41. Onisei, S.; Pontikes, Y.; Van Gerven, T.; Angelopoulos, G.N.; Velea, T.; Predica, V.; Moldovan, P. Synthesis of inorganic polymers using fly ash and primary lead slag. *J. Hazard. Mater.* **2012**, *205–206*, 101–110. [[CrossRef](#)] [[PubMed](#)]

42. Muñoz-Villarreal, M.S.; Manzano-Ramírez, A.; Sampieri-Bulbarela, S.; Gasca-Tirado, J.R.; Reyes-Araiza, J.L.; Rubio-Ávalos, J.C.; Pérez-Bueno, J.J.; Apatiga, L.M.; Zaldivar-Cadena, A.; Amigó-Borrás, V. The effect of temperature on the geopolymerization process of a metakaolin-based geopolymer. *Mater. Lett.* **2011**, *65*, 995–998. [[CrossRef](#)]
43. Sindhunata; van Deventer, J.S.J.; Lukey, G.C.; Xu, H. Effect of Curing Temperature and Silicate Concentration on Fly-Ash-Based Geopolymerization. *Ind. Eng. Chem. Res.* **2006**, *45*, 3559–3568. [[CrossRef](#)]
44. Roelofs, J.C.A.A.; Lensveld, D.J.; van Dillen, A.J.; de Jong, K.P. On the Structure of Activated Hydrotalcites as Solid Base Catalysts for Liquid-Phase Aldol Condensation. *J. Catal.* **2001**, *203*, 184–191. [[CrossRef](#)]
45. Alzeer, M.I.M.; MacKenzie, K.J.D.; Keyzers, R.A. Porous aluminosilicate inorganic polymers (geopolymers): A new class of environmentally benign heterogeneous solid acid catalysts. *Appl. Catal. A Gen.* **2016**, *524*, 173–181. [[CrossRef](#)]
46. Mozgawa, W.; Deja, J. Spectroscopic studies of alkaline activated slag geopolymers. *J. Mol. Struct.* **2009**, *924–926*, 434–441. [[CrossRef](#)]
47. Heinrich, F.; Schmidt, C.; Löffler, E.; Menzel, M.; Grünert, W. Fe-ZSM-5 Catalysts for the Selective Reduction of NO by Isobutane—The Problem of the Active Sites. *J. Catal.* **2002**, *212*, 157–172. [[CrossRef](#)]
48. Waijarean, N.; MacKenzie, K.J.D.; Asavapisit, S.; Piyaphanuwat, R.; Jameson, G.N.L. Synthesis and properties of geopolymers based on water treatment residue and their immobilization of some heavy metals. *J. Mater. Sci.* **2017**, *52*, 7345–7359. [[CrossRef](#)]
49. Gabrienko, A.A.; Danilova, I.G.; Arzumanov, S.S.; Toktarev, A.V.; Freude, D.; Stepanov, A.G. Strong acidity of silanol groups of zeolite beta: Evidence from the studies by IR spectroscopy of adsorbed CO and ¹H MAS NMR. *Microporous Mesoporous Mater.* **2010**, *131*, 210–216. [[CrossRef](#)]
50. Sahu, P.K. A green approach to the synthesis of a nano catalyst and the role of basicity, calcination, catalytic activity and aging in the green synthesis of 2-aryl bezimidazoles, benzothiazoles and benzoxazoles. *RSC Adv.* **2017**, *7*, 42000–42012. [[CrossRef](#)]
51. Mao, W.; Ma, H.; Wang, B. A clean method for solvent-free nitration of toluene over sulfated titania promoted by ceria catalysts. *J. Hazard. Mater.* **2009**, *167*, 707–712. [[CrossRef](#)]
52. Yunsheng, Z.; Wei, S.; Qianli, C.; Lin, C. Synthesis and heavy metal immobilization behaviors of slag based geopolymer. *J. Hazard. Mater.* **2007**, *143*, 206–213. [[CrossRef](#)] [[PubMed](#)]
53. Lee, W.K.W.; van Deventer, J.S.J. Use of Infrared Spectroscopy to Study Geopolymerization of Heterogeneous Amorphous Aluminosilicates. *Langmuir* **2003**, *19*, 8726–8734. [[CrossRef](#)]
54. Lei, Y.; Huo, J.; Liao, H. Fabrication and catalytic mechanism study of CeO₂-Fe₂O₃-ZnO mixed oxides on double surfaces of polyimide substrate using ion-exchange technique. *Mater. Sci. Semicond. Process.* **2018**, *74*, 154–164. [[CrossRef](#)]
55. Lei, Y.; Huo, J.; Liao, H. Microstructure and photocatalytic properties of polyimide/heterostructured NiO-Fe₂O₃-ZnO nanocomposite films via an ion-exchange technique. *RSC Adv.* **2017**, *7*, 40621–40631. [[CrossRef](#)]
56. Lu, L.; Li, J.; Ng, D.H.L.; Yang, P.; Song, P.; Zuo, M. Synthesis of novel hierarchically porous Fe₃O₄@MgAl-LDH magnetic microspheres and its superb adsorption properties of dye from water. *J. Ind. Eng. Chem.* **2017**, *46*, 315–323. [[CrossRef](#)]
57. Fajerwerg, K.; Debellefontaine, H. Wet oxidation of phenol by hydrogen peroxide using heterogeneous catalysis Fe-ZSM-5: A promising catalyst. *Appl. Catal. B Environ.* **1996**, *10*, L229–L235. [[CrossRef](#)]
58. Centi, G.; Perathoner, S.; Torre, T.; Verduna, M.G. Catalytic wet oxidation with H₂O₂ of carboxylic acids on homogeneous and heterogeneous Fenton-type catalysts. *Catal. Today* **2000**, *55*, 61–69. [[CrossRef](#)]
59. Yan, Y.; Jiang, S.; Zhang, H. Catalytic wet oxidation of phenol with Fe-ZSM-5 catalysts. *RSC Adv.* **2016**, *6*, 3850–3859. [[CrossRef](#)]
60. Arnold, S.M.; Hickey, W.J.; Harris, R.F. Degradation of Atrazine by Fenton's Reagent: Condition Optimization and Product Quantification. *Environ. Sci. Technol.* **1995**, *29*, 2083–2089. [[CrossRef](#)]
61. Hua, Z.; Ma, W.; Bai, X.; Feng, R.; Yu, L.; Zhang, X.; Dai, Z. Heterogeneous Fenton degradation of bisphenol A catalyzed by efficient adsorptive Fe₃O₄/GO nanocomposites. *Environ. Sci. Pollut. Res.* **2014**, *21*, 7737–7745. [[CrossRef](#)]
62. Argyle, M.D.; Bartholomew, C.H. Heterogeneous Catalyst Deactivation and Regeneration: A Review. *Catalysts* **2015**, *5*, 145–269. [[CrossRef](#)]
63. Han, E.; Vijayarangamuthu, K.; Youn, J.; Park, Y.; Jung, S.; Jeon, K. Degussa P25 TiO₂ modified with H₂O₂ under microwave treatment to enhance photocatalytic properties. *Catal. Today* **2018**, *303*, 305–312. [[CrossRef](#)]
64. Liu, J.; Xiong, Z.; Zhou, F.; Lu, W.; Jin, J.; Ding, S. Promotional effect of H₂O₂ modification on the cerium-tungsten-titanium mixed oxide catalyst for selective catalytic reduction of NO with NH₃. *J. Phys. Chem. Solids* **2018**, *121*, 360–366. [[CrossRef](#)]
65. Heponiemi, A.; Azalim, S.; Hu, T.; Vielma, T.; Lassi, U. Efficient removal of bisphenol A from wastewaters: Catalytic wet air oxidation with Pt catalysts supported on Ce and Ce-Ti mixed oxides. *AIMS Mater. Sci.* **2019**, *6*, 25–44. [[CrossRef](#)]
66. Seaton, N.A.; Walton, J.P.R.B.; Quirke, N. A new analysis method for the determination of the pore size distribution of porous carbons from nitrogen adsorption measurements. *Carbon* **1989**, *27*, 853–861. [[CrossRef](#)]